Electronic Supplementary Material (ESI) for Journal of Materials Chemistry A.

Supplementary Information

Achieving a Fine Balance between Strong Mechanical and High Thermoelectric Properties of *n*-type PbTe-3%Sb Materials by Alloying PbS

Liangwei Fu[a,b], Juan Cui[a,c], Yong Yu[a], Yi Huang[a], Yifan Wang[a], Yue Chen[c] and Jiaqing He*[a]

[a]Shenzhen Key Laboratory of Thermoelectric Materials and Department of Physics, University of Science and Technology, Shenzhen 518055, China, *E-mail: he.jq@sustc.edu.cn.

[b]Key Laboratory of Artificial Micro- and Nano-Structures of Ministry of Education and School of Physics and Technology, Wuhan University, Wuhan 430072, China.

[c]Department of Mechanical Engineering, The University of Hong Kong, Pokfulam Road, Hong Kong SAR, China.

Table of Contents

Results and Discussion.

1 Computational details of density functional theory (DFT)

In this work, we conducted density functional theory (DFT) calculations using the Vienna ab initio simulation package (VASP) [1]. The Perdew–Burke–Ernzerhof (PBE) generalized gradient approximation (GGA) [2] was applied as the exchange–correlation functional. We constructed a 3×3×3 supercell of PbTe containing 54 atoms and substituted one Te atoms with S to simulate the $Pb_{27}Te_{26}S$ alloy. The cutoff energy for plane wave was set to 350 eV and the *k*-point mesh density was set to $2\pi\times0.03$ $Å^{-1}$ using the Γ-centered Monkhorst-Pack scheme [3]. The energy convergence criterion was set to 10^{-6} eV. The structures were fully relaxed before non-self-consistent band structure calculations, where the spin-orbit coupling (SOC) effect was included. The decomposed charge density was calculated for the electrons near conduction band minimum (CBM), corresponding to an n-type carrier concentration of 5×10^{19} cm^{-3}. The elastic constants (C_{ij}) of $PbTe_{1-x}S_x$ were calculated using a conventional unit cell containing 8 atoms by employing a larger cutoff energy of 400 eV and the virtual crystal approximation (VCA) scheme [4]. The moduli of the corresponding polycrystalline $PbTe_{1-x}S_x$ alloys were calculated by adopting the Voigt-Reuss-Hill approximation [5].

2 Modelling on the electrical transport properties

To estimate the band parameters more precisely, the Hall factors, $A=A_kA_\tau$,[6] allows the anisotropy effect for conduction band, which is chosen to be a constant of 0.9 (corresponding to a mass anisotropy factor of K=3.58). A_τ measures the degeneracy of carriers and was adopted as 1 in the calculation, regardless of the scattering mechanism of carriers. The room temperature density of states effective mass (m^*) is $0.25m_e$ and is considered as composition independent based on the band structure calculation. The degeneracy of the bottom of conduction band (N_v) equals 4. The m^* depends on temperature via $\Delta=d\ln m^*/d\ln T=0.5$ for the conduction band. The temperature (T in Kelvins) dependence of energy gap (E_g) is given by E_g=0.18+4T/1000 (eV). The deformation potential coefficients (E_{def}) for acoustic phonon in conduction band of PbTe and PbS are 22 eV and 27 eV [7], respectively and are considered as temperature independent. For $PbTe_{1-x}S_x$-3%Sb-$I_{0.004}$ (x=0.05, 0.10, 0.15) samples, the deformation potential coefficients are estimated by a mole average of the E_{def} values for PbTe and PbS. Thus, the deformation potential coefficients are 22.25 eV, 22.5 eV, 22.75 eV for x=0.05, 0.01, 0.15 samples, respectively. The combined elastic modulus (C_l) is calculated by $C_l=v_L^2d$, where d and v_L are the mass density and longitudinal phonon speed, respectively. In the equations for drift mobility the integral is defined by[8]:

$$ {}^nF_k^m = \int_0^\infty \left(-\frac{\partial f}{\partial \varepsilon} \right) \varepsilon^n \left(\varepsilon + \alpha\varepsilon^2 \right)^m \left[\left(1+2\alpha\varepsilon \right)^2 + 2 \right]^{k/2} d\varepsilon \tag{S1} $$

Where f is the Fermi-Dirac distribution function, $\varepsilon=E/k_BT$ is reduced charge carrier energy and $\alpha=k_BT/E_g$ is the nonparabolicity parameters. All the room temperature parameters used in the calculation are listed in the Table S2 below.

3 Discussion on the carrier mobility

From Figure S6a and S6b, we observe that the electron concentration of the PbTe-3%Sb-$I_{0.004}$ sample remains nearly unchanged, while the Hall mobility decreases dramatically after alloying PbS, as indicated by the black dashed ellipse in Figure S7b, which is the exact reason for the decrease in electrical conductivity at room temperature. To determine the mechanism behind this phenomenon, we use the SKB model to calculate the theoretical mobility by considering the acoustic phonon scattering, grain-boundary scattering, and alloy disorder scattering. First, the Hall mobility (μ_H) versus carrier concentration (n) curve at 300 K is calculated based on deformation-potential theory. When acoustic phonon scattering dominates, the drift mobility μ is expressed as[9]

$$\mu_{AP} = \frac{2\pi\hbar e C_l}{m_l^* \left(2m_b^* k_B T\right)^{3/2} E_{def}^2} \frac{3\,{}^0F_{-2}^1}{{}^0F_0^{3/2}}, \tag{S2}$$

where $\hbar$, k_B, C_l, m_I*, m_b*, and E_{def} are the reduced Planck constant, Boltzmann constant, combined elastic modulus, inertial effective mass, single-valley effective mass, and deformation potential coefficient, respectively. ${}^nF_l^m$ is the generalized Fermi integral, the definition by Equation S1. And the values of parameters used in this model are shown in Table S2. The drift mobility (μ) is related to the Hall mobility (μ_H) via $\mu_H = A\mu$, where A is the Hall factor[10]. As shown in Figure S6b, the calculated line (black solid line) fits well with the experimental results of single-phase PbTe in Ref. [11], which confirms the validity of this theory.

It is noteworthy that the Hall mobility of our PbS-free sample is slightly lower than that of iodine-doped PbTe with the same carrier concentration. This discrepancy might be attributed to grain-boundary scattering, by considering the ball milling process before sintering in our sample synthesis process, which would result in a large interface density. The drift mobility with grain-boundary scattering (μ_{GB}) is given by[12]

$$\mu_{GB} = De\left(\frac{1}{2\pi m_b^* k_B T}\right)^{1/2} \exp\left(-\frac{E_B}{k_B T}\right) \tag{S3}$$

where D, m_b*, and E_B are the grain size obtained from EBSD analysis, single-valley effective mass, and potential barrier, respectively. E_B is the most important parameter characterizing grain-boundary scattering, which is an undetermined variable. To obtain the value of E_B, we conducted low-temperature Hall measurements, and the results are shown in Figure S6c. As is well known, if electron scattering is dominated by acoustic phonons, the Hall mobility μ_H will exhibit a $T^{-1.5}$ dependence[10]. However, the experimental mobility of PbTe-3%SbI$_{0.004}$ increases much more slowly with deceasing temperature, following a $T^{-0.76}$ trend rather than a $T^{-1.5}$ trend, which implies that other electron-scattering effects may exist, consistent with the existence of grain-boundary scattering, which we suspected. Combining the two scattering mechanisms (acoustic phonon and grain boundary) according to the Matthiessen's rule yields the expression for the overall drift mobility (μ):

$$\mu^{-1} = \mu_{AP}^{-1} + \mu_{GB}^{-1}. \tag{S4}$$

The E_B value of 0.055 eV is obtained by fitting the experimental mobility values of the PbTe-3%Sb-I$_{0.004}$ sample, which is reasonable when compared with the literature values[13]. The calculated overall μ_H for PbTe-3%Sb-I$_{0.004}$ in Figure S6c is well consistent with the experimental values at 200–300 K. When temperature decreases below 200 K, the calculated Hall mobility for the PbTe-3%Sb-I$_{0.004}$ sample starts to decrease rapidly because the room-temperature values of E_{def}, C_l, and E_b are used in the calculation of low-temperature mobility, while actually they are only reasonable near room temperature.

The Hall mobility of PbTe$_{0.85}$S$_{0.15}$-3%Sb-I$_{0.004}$ exhibits a $T^{-0.5}$ trend with decreasing temperature (Figure S6c), which indicates the dominance of alloy scattering[10]. Therefore, we must include the contribution from alloy scattering (μ_{AL}) to explain the behavior of Hall mobility after alloying PbS. The drift mobility due to alloy scattering is given by[14, 15]

$$\mu_{AL} = \frac{8\hbar^4 e}{3\sqrt{2}\pi\Omega x(1-x)E_{al}{}^2 m_b^{*3/2} m_l^* (k_B T)^{1/2}} \frac{3\,{}^0F_{-2}^1}{{}^0F_0^{3/2}}, \tag{S5}$$

where Ω, x, and E_{al} are the volume per atom, percentage of substituted atoms, and alloy scattering potential, respectively. The alloy scattering potential E_{al} measures the ability of alloy scattering. For PbTe$_{1-x}$S$_x$-3%Sb-

$I_{0.004}$ (x>0.00), we assume that the values of E_B and m_b* are the same as for PbTe–3%Sb-$I_{0.004}$. By applying an E_{al} of 2 eV, the calculated Hall mobility values can roughly simulate the experimental results within a 15% error bar, as shown in Figure S6d. The fitted E_{al} value for $PbTe_{1-x}S_x$-3%Sb-$I_{0.004}$ (x>0.00) is relatively larger than that for the *n*-type $(PbTe)_{1-x}(PbSe)_x$ system[16] (approximately 1.1 eV) and many other alloy systems[16]. The large E_{al} of PbTe–PbS alloys may be due to the large electron-affinity difference (~1.2 eV) between PbTe (4.6 eV) and PbS (3.4 eV).

To deeply understand the obvious mobility reduction of PbTe after alloying PbS and the large E_{al} value, theoretical charge densities of pure PbTe and PbTe–PbS alloy were calculated based on DFT and the calculated contour plots of the (1 −1 0) plane are shown in Figure S7. In pure PbTe, as shown in Figure S8a, lead and tellurium atoms form columns via ionic–covalent mixed bonds due to the small electronegativity difference (~0.23) between Pb and Te. As a binary semiconductor, the covalence feature of the Pb–Te bonds can partly account for the high-mobility nature of PbTe[17]. On the contrary, owing to the larger electronegativity difference (~0.71) between lead and sulfur atoms, the Pb-S bond is more ionic than the Pb–Te bond. Therefore, charge density is more localized around sulfur atoms and the covalent-like links in lead- and tellurium-atom columns are broken, as clearly shown in Figure S8b. This phenomenon is also shown by the electron localization function (ELF) (Figure S8). Therefore, we argue that the substantial disturbance of the charge-density distribution can serve as an origin of the large E_{al} values of PbS alloying in PbTe.

4 Supplementary tables and figures (Table S1 and S2, Figure S1-S11)

Table S1 Elastic constants (C_{ij}, in GPa) and lattice parameters (a in Å) of $PbTe_{1-x}S_x$ alloys calculated from DFT. Bulk moduli (B, in GPa), shear moduli (G, in GPa), and Young's moduli (E, in GPa) of polycrystalline $PbTe_{1-x}S_x$ alloys calculated adopting the VRH approximation.

x	C_{11}	C_{12}	C_{44}	*B*	*G*	*E*	*B*/*G*	*a*
0	106.94	6.05	14.30	39.68	24.40	60.74	1.63	6.56
0.05	106.99	6.60	14.36	40.06	24.40	60.84	1.64	6.54
0.1	107.66	7.25	14.42	40.72	24.45	61.12	1.67	6.52
0.15	107.39	7.45	14.51	40.76	24.48	61.18	1.67	6.50
0.2	107.56	7.76	14.64	41.03	24.58	61.46	1.67	6.48
0.4	110.92	10.11	15.29	43.71	25.27	63.55	1.73	6.37
0.6	115.45	11.79	16.40	46.34	26.57	66.92	1.74	6.26
0.8	122.64	15.19	17.90	51.01	28.32	71.70	1.80	6.14
1	130.41	17.07	20.40	54.85	31.16	78.61	1.76	6.00

Table S2 room temperature parameters used in the calculation of Hall mobility of the PbTe-3%Sb-$I_{0.004}$ sample.

Parameters	values
Hall factor *A*	0.9
Band degeneracy *Nv*	4
Density of states effective mass $m^*=N_v^{2/3}m_{d1}^*$	0.25 m_e
Inertial or conducting effective mass $m_I=3(1/m_l^*+2/m_t^*)^{-1}$	0.8604 m_{d1}^*

Single valley effective mass m_{d1}*	0.0992 m_e
Energy gap E_g	0.3 eV
Mass anisotropy factor $K=m_l^*/m_t^*$	3.58
Deformation potential coefficient for acoustic E_{def}	22 eV
Grain size D	1300 nm
Potential barrier at grain boundary E_B	0.05 eV
Alloy scattering potential E_{al}	2 eV
Volume per atom Ω	33.7923 $Å^3$

Figure S1~S13

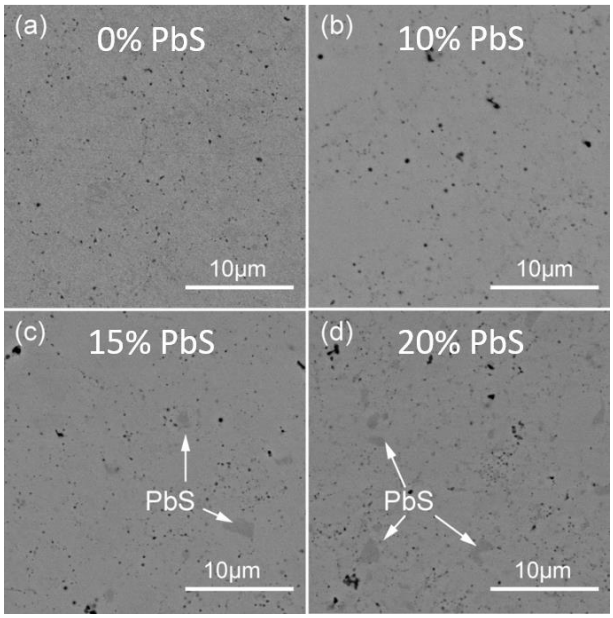

Figure S1 a-d the back scattering electron (BSE) images of $PbTe_{1-x}S_x$-3%Sb-$I_{0.004}$ (x=0.00, 0.10, 0.15 and 0.20) samples, respectively. Apparent PbS phases in micrometres size appeared when x exceeds 10%.

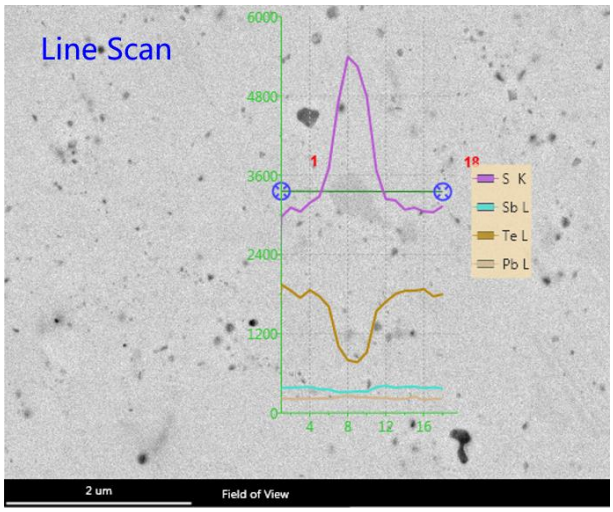

Figure S2 the EDS line analysis of $PbTe_{0.85}S_{0.15}$-3%Sb-$I_{0.004}$ sample. The area with dark contrast is rich in sulfur and lack lead, which is PbS phase according to the XRD results.

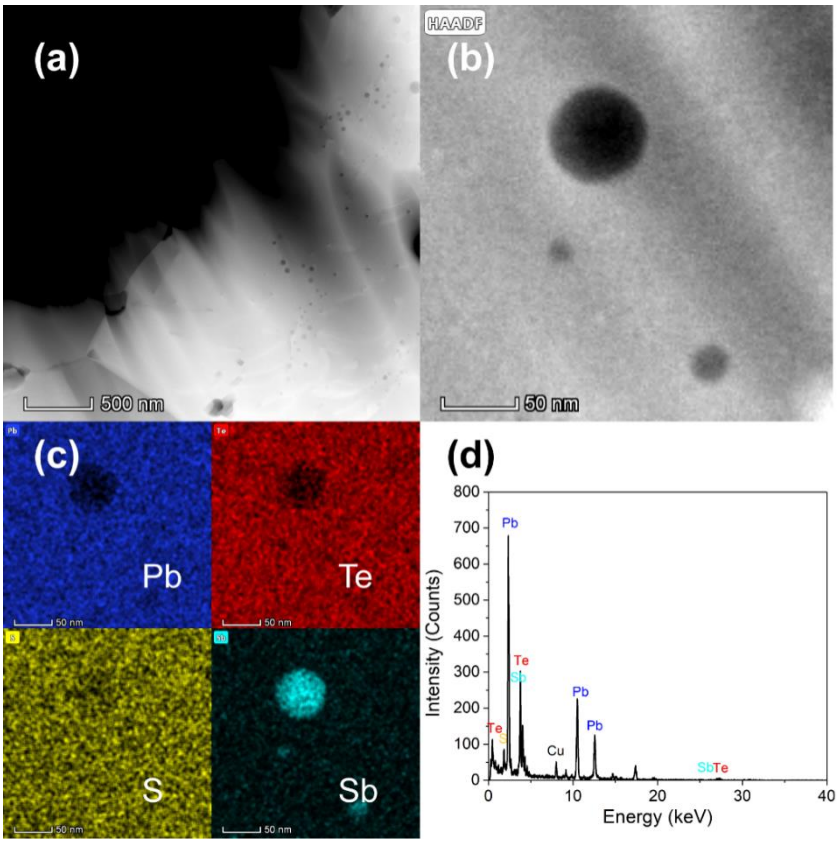

Figure S3 (a) a low magnified HAADF mode image of the $PbTe_{0.90}S_{0.10}$-3%Sb-$I_{0.004}$ sample, (b) a typical area in (a) containing three nano particles with dark contrast, (c) the EDS mapping analysis of the area shown in (b), (d) the energy dispersive spectrometer (EDS) spectrum. The appearance of peaks in the spectrum corresponding to cooper is due to the copper supporting ring.

Figure S4a shows one typical region in $PbTe_{0.9}S_{0.1}$-3%Sb-$I_{0.004}$, where three grains are separated by boundaries. Figure S4b are the fast Fourier transformation (FFT) patterns of the areas in grain A and B indicated by the yellow and blue boxes, respectively. These two sets of patterns correspond to the same zone axis and only rotate a very small angle with each other, which is a solid evidence showing that the boundary separating grain A and B is a low angle boundary. The small orientation difference between grain A and B may account for their different contrast in the HRTEM mode.

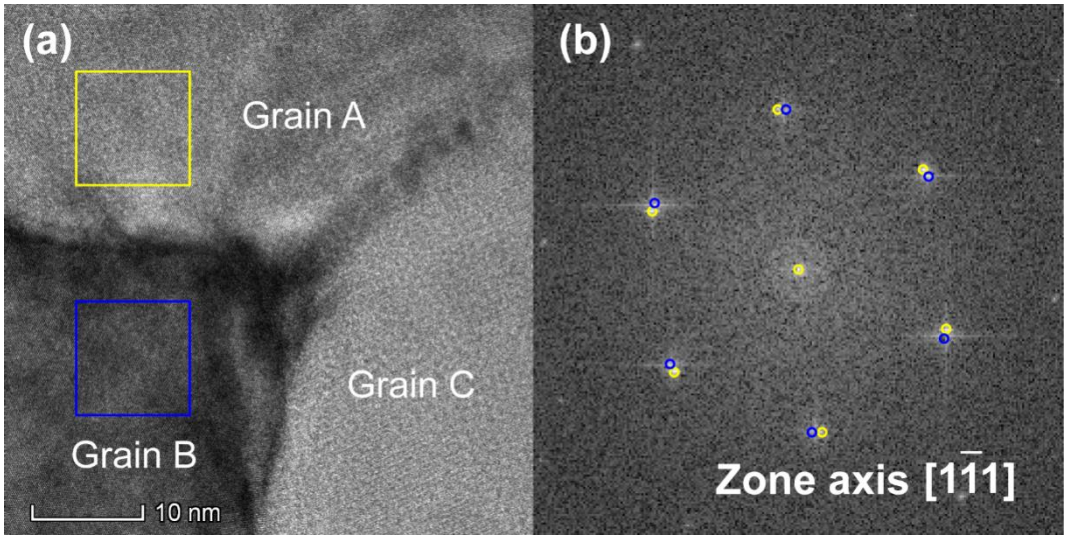

Figure S4 (a) the HRTEM image of one typical region $PbTe_{0.9}S_{0.1}$-3%Sb-$I_{0.004}$ sample. (b) the fast Fourier transformation (FFT) pattern of two areas indicated in Figure 4a by a yellow and a blue box, respectively.

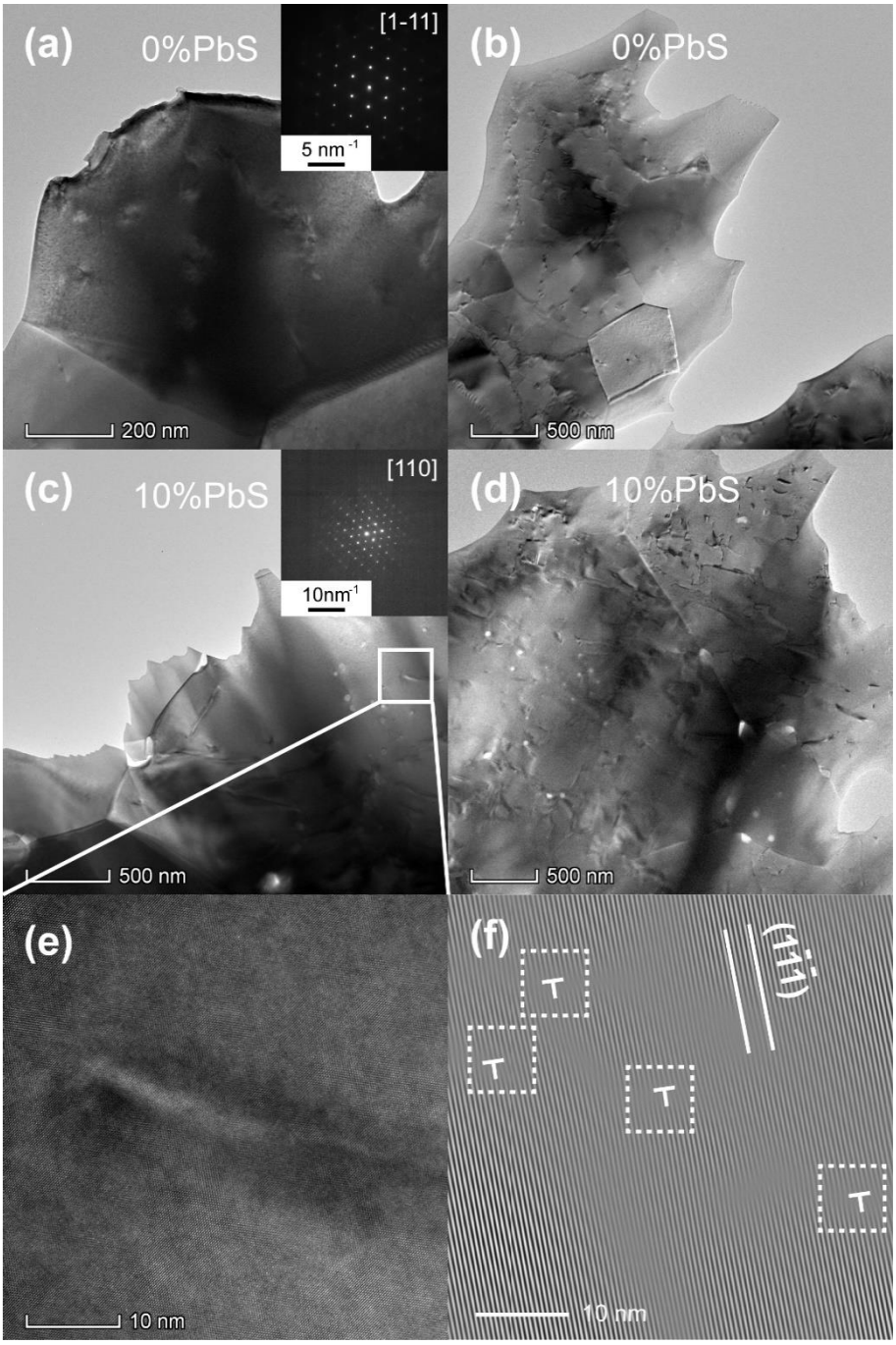

Figure S5 (a)-(d) the low magnified TEM images of the reference and the $PbTe_{0.90}S_{0.10}$-3%Sb-$I_{0.004}$ sample, respectively. The zone axis of (a) and (c) are [1-11] and [110], respectively. (e) the HRTEM image of the selected area in (c), which shows a line with black and white contrast. (f) the FFT pattern of (e). To make it easy to see, the Fig. S7f are magnified and several obvious dislocations are indicated by white dashed box.

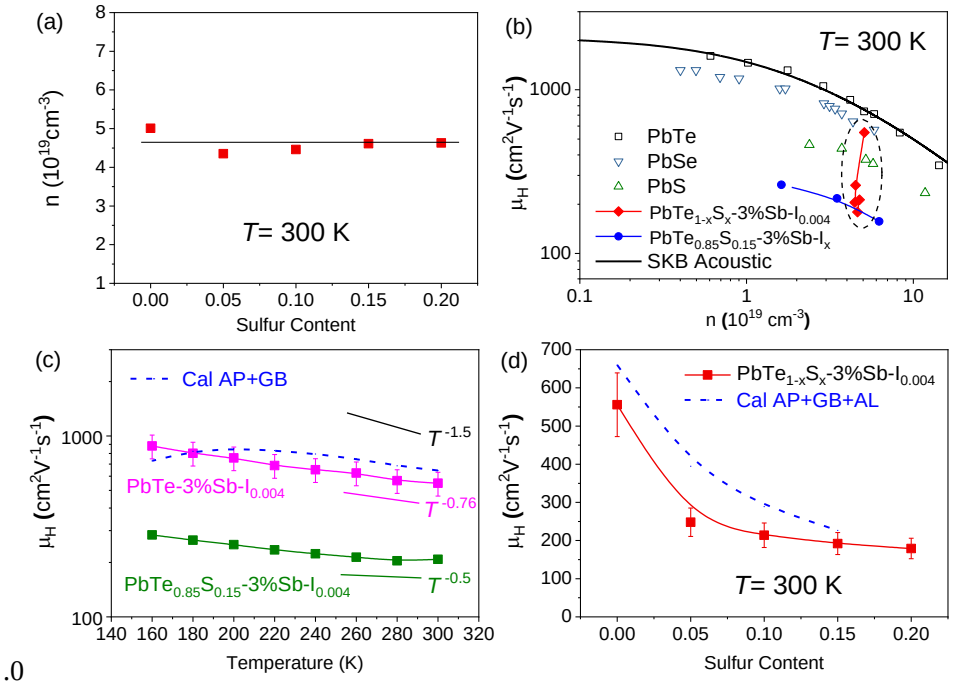

.0

Figure S6 (a,d) Sulfur-content dependence of electron concentration and Hall mobility for $PbTe_{1-x}S_x$-3%Sb-$I_{0.004}$ (x=0, 0.05, 0.10, 0.15, and 0.20) samples at 300 K, respectively. Blue dashed line in (d) is calculated based on SKB model only considering three phonon-scattering mechanisms. (b) Hall mobility vs carrier concentration curve at 300 K for $PbTe_{1-x}S_x$-3%Sb-$I_{0.004}$ (x=0, 0.05, 0.10, 0.15, and 0.20) and $PbTe_{0.85-x}S_{0.15}$-3%Sb-I_x (x=0.000, 0.002, 0.004, and 0.006) samples. Some reported values of PbTe[11], PbSe[18], and PbS[7] are also included for comparison. Black line is calculated based on SKB model only considering the acoustic scattering. (c) Temperature dependence of Hall mobility for reference and $PbTe_{0.85}S_{0.15}$-3%Sb-$I_{0.004}$ samples from 160 to 300 K. Blue dashed line in (c) is calculated based on SKB model considering both acoustic and grain-boundary scattering.

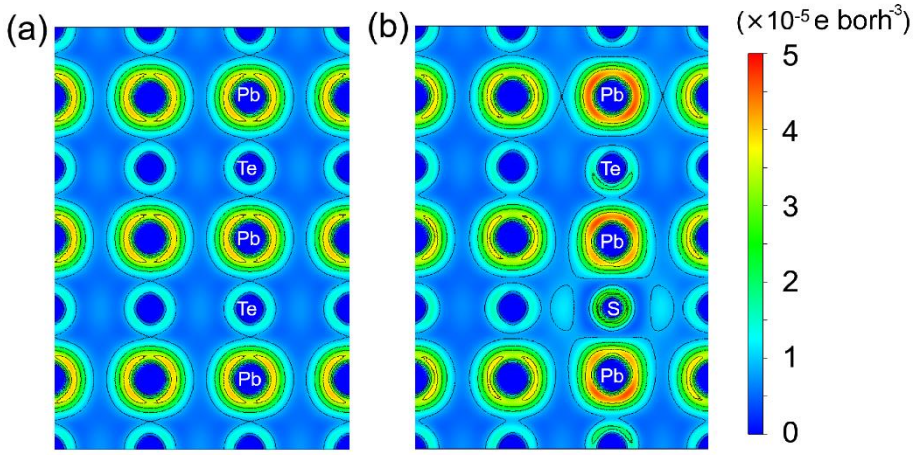

Figure S7 Decomposed charge density on the (1 −1 0) plane of (a) pristine PbTe and (b) $Pb_{27}Te_{26}S$, corresponding to an electron concentration of 5×10^{19} cm^{-3}.

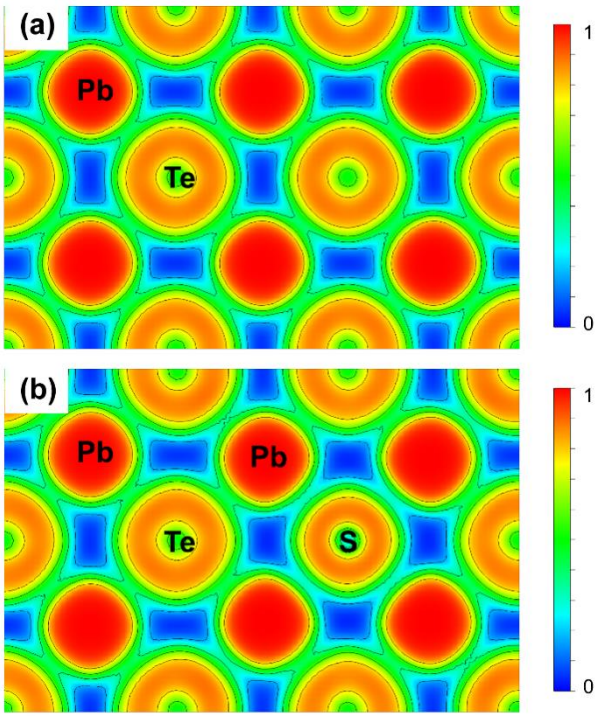

Figure S8 the ELF plot of the (110) crystal plane of the pristine and S-doped PbTe calculated using a 3×3×3 supercell. As can be seen in the Figure S7(b), the bond of Pb-S is more ionic than that of Pb-Te bond.

Figure S9 shows the band structures and density of states of pure PbTe and PbTe-PbS alloys. PbTe is a semiconductor with a direct gap of about 0.18eV, which is consistent with the reported results. It is noted that the band gap is a little smaller than the experimental results, which is due to the underestimation of energy gap via first-principles calculation. The conduction band is mainly contributed from Pb atoms while the valence band is mainly contributed from Te atoms. After alloying with PbS, the shapes of the bottom of conduction band and the top of valence band are unchanged, which implies that the density-of-state effective mass of conduction band will not change much after alloying PbS. As $PbTe_{1-x}S_x$-3%Sb-$I_{0.004}$ (x=0.00, 0.05, 0.10, 0.15 and 0.20) samples have similar electron concentration, it is normal that we did not observe any obvious change in Seebeck coefficient.

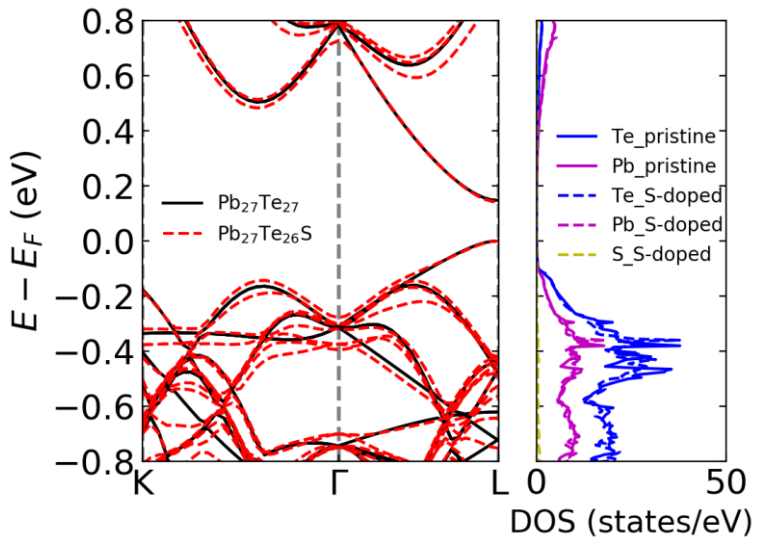

Figure S9 Band structures of the pristine and S-doped PbTe calculated using a 3×3×3 supercell. It is seen that the electron effective mass at the CBM at L point is almost unaffected by S alloying.

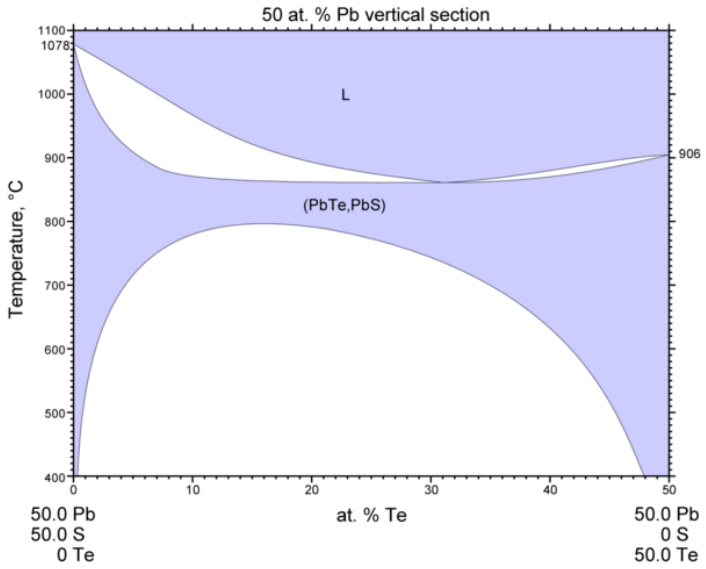

Figure S10 The pseudobinary diagram of PbS and PbTe

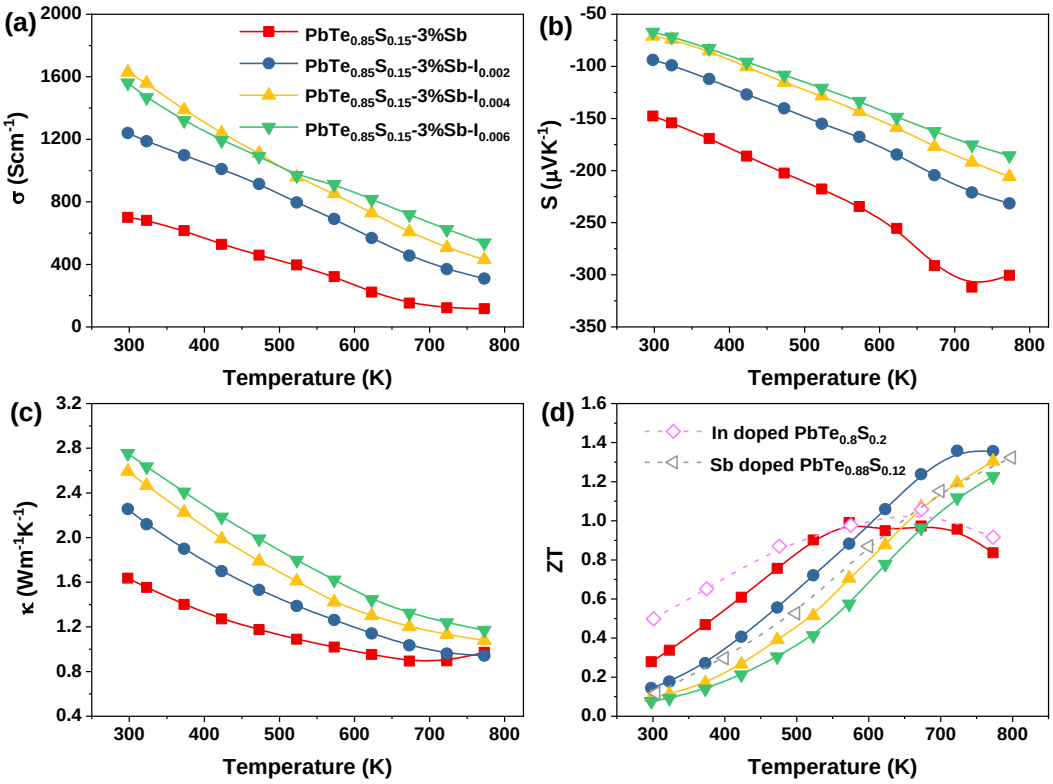

Figure S11 the temperature dependence of the thermoelectric properties of $PbTe_{0.85}S_{0.15}$-3%Sb-I_x (x=0.000, 0.002, 0.004 and 0.006) samples. (a) Electrical conductivity, (b) Seebeck coefficient, (c) total thermal conductivity and (d) dimensionless thermoelectric figure of merit (*ZT*). The reported indium doped $PbTe_{0.8}S_{0.2}$ and Sb doped $PbTe_{0.88}S_{0.12}$ samples are also shown for comparison.

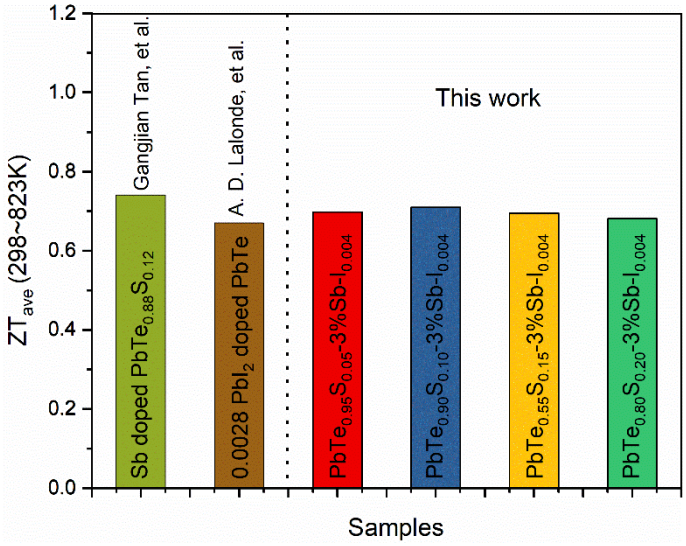

Figure S12 The comparison of averaged *ZT* values between this work and literatures.

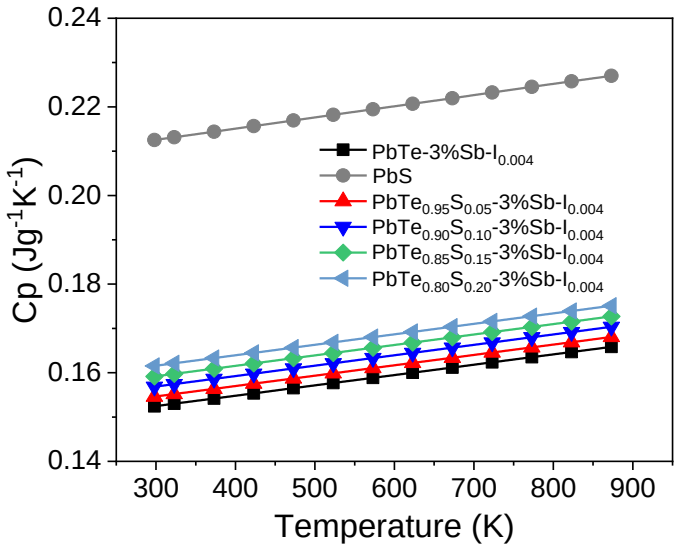

Figure S13 the heat capacity of the reference sample, $PbTe_{1-x}S_x$-3%Sb-$I_{0.004}$ (x=0.05, 0.10, 0.15, 0.20) and PbS. The heat capacity C_p of PbTe-3%Sb and PbS are determined using the equation C_p/k_B atom^{-1} =3.07+4.7×10^{-4}(T/K-300) for lead chalcogenides. The total C_p of $PbTe_{1-x}S_x$-3%Sb-$I_{0.004}$ (C_p(x)) (x=0, 0.05, 0.10, 0.15, 0.20) was estimated by a mass average of the temperature dependent specific heat values for PbTe and PbS, which is described in the manuscript in detail.

References

1. G. Kresse and J. Furthmüller, *Phys. Rev. B*, 1996, **54**, 11169-11186.
2. J. P. Perdew, K. Burke and M. Ernzerhof, *Physical Review Letters*, 1996, **77**, 3865-3868.
3. H. J. Monkhorst and J. D. Pack, *Phys. Rev. B*, 1976, **13**, 5188-5192.
4. L. Bellaiche and D. Vanderbilt, *Phys. Rev. B*, 2000, **61**, 7877-7882.
5. O. L. Anderson, in *Physical Acoustics*, ed. W. P. Mason, Academic Press, 1965, vol. 3, pp. 43-95.
6. Y. Pei, X. Shi, A. LaLonde, H. Wang, L. Chen and G. J. Snyder, *Nature*, 2011, **473**, 66-69.
7. H. Wang, E. Schechtel, Y. Pei and G. J. Snyder, *Adv. Energy Mater.*, 2013, **3**, 488-495.
8. Y. Pei, H. Wang, Z. M. Gibbs, A. D. LaLonde and G. J. Snyder, *NPG Asia Materials*, 2012, **4**, e28.
9. X. J. Tan, H. Z. Shao, J. He, G. Q. Liu, J. T. Xu, J. Jiang and H. C. Jiang, *Phys. Chem. Chem. Phys.*, 2016, **18**, 7141-7147.

10. H. Xie, H. Wang, Y. Pei, C. Fu, X. Liu, G. J. Snyder, X. Zhao and T. Zhu, *Adv. Funct. Mater.*, 2013, **23**, 5123-5130.

11. A. D. LaLonde, Y. Pei and G. J. Snyder, *Energy Environ. Sci.*, 2011, **4**, 2090.

12. R. He, D. Kraemer, J. Mao, L. Zeng, Q. Jie, Y. Lan, C. Li, J. Shuai, H. S. Kim, Y. Liu, D. Broido, C.-W. Chu, G. Chen and Z. Ren, *Proc. Natl. Acad. Sci.*, 2016, **113**, 13576-13581.

13. J. Martin, L. Wang, L. Chen and G. S. Nolas, *Phys. Rev. B*, 2009, **79**, 115311.

14. H. Wang, J. Wang, X. Cao and G. J. Snyder, *J. Mater. Chem. A*, 2014, **2**, 3169-3174.

15. D. Wu, L.-D. Zhao, S. Hao, Q. Jiang, F. Zheng, J. W. Doak, H. Wu, H. Chi, Y. Gelbstein, C. Uher, C. Wolverton, M. Kanatzidis and J. He, *J. Am. Chem. Soc.*, 2014, **136**, 11412-11419.

16. H. Wang, A. D. LaLonde, Y. Pei and G. J. Snyder, *Adv. Funct. Mater.*, 2013, **23**, 1586-1596.

17. E. S. Toberer, A. F. May and G. J. Snyder, *Chem. Mater.*, 2010, **22**, 624-634.

18. H. Wang, Y. Pei, A. D. LaLonde and G. J. Snyder, *Proc. Natl. Acad. Sci.*, 2012, **109**, 9705-9709.